Journal of
Synchrotron Radiation

ISSN 0909-0495

Received 21 June 2005
Accepted 21 October 2005

Characterization of X-ray area detectors for synchrotron beamlines

Cyril Ponchut

European Synchrotron Radiation Facility, Grenoble, France. E-mail: ponchut@esrf.fr

In order to deal with the problem of quantitative and consistent evaluation of two-dimensional X-ray detectors at synchrotron beamlines, the methodology for X-ray area detector characterization is reviewed. It is based on the definition of a minimum yet complete set of imaging parameters able to describe any kind of two-dimensional detector regardless of its operating range, field of application and detecting principle. Measuring and derivation methods are reviewed for each parameter. Imaging parameters are to a large extent directly exploitable to assess the performance of a detector for any scientific application. Imaging characterization aims at helping two-dimensional detector developers and two-dimensional detector users in defining or choosing the device best suited for a given application, based on quantitative arguments.

Keywords: X-ray imaging; MTF; DQE; NPS.

1. Introduction

X-ray area detectors are used in nearly every scientific domain on synchrotron beamlines, not only in diffraction or imaging but also in spectroscopy in association with energy-dispersive optics. One reason for their widespread use is that they come in a variety of formats and characteristics allowing them to fit a wide range of applications. Another major reason is the time saved by one-shot two-dimensional data collection in comparison with space or energy scanning with a dimensionless detector. This allows for time-resolved experiments that could not be performed otherwise, as well as for more efficient beam-time use. The latter aspect is of importance for a synchrotron facility if considering the number of rejected experiment proposals owing to a lack of beam time.

At the time of this review, CCD-based systems represent more than 90% of the X-ray area detectors on ESRF beamlines, others being essentially image-plate scanners and multiwire gas-filled chambers. The hegemony of CCD systems relies on their extreme versatility, allowing coverage from submicrometric to millimetric spatial resolution, as well as on the high reliability of commercial CCD cameras and systems. Imaging-plate online scanners are cost-efficient systems for experiments without need for high acquisition speeds and in some cases can serve as spares to replace large CCD systems. Photon-counting gas-filled multiwire chambers are used for static experiments requiring single photon detection with relatively large area (Lewis *et al.*, 1997; Koch, Boulin *et al.*, 2001). Besides these systems, novel array detector technologies are nowadays becoming available for synchrotron experiments, like amorphous silicon large-area flat panels and photon-counting pixel arrays, with performances sometimes exceeding those of CCD systems, as well as with new detection features extending the range of applications (Bérar *et al.*, 2002; Broennimann *et al.*, 2003; Ponchut & Zontone, 2003).

This heterogeneous landscape can make it difficult for a user to select the right detector for an experiment. Even among a given category like CCD detectors the wide range of systems, as well as the sometimes inconsistent and often incomplete commercial specifications, can make a selection difficult. In order to check whether a detector is meeting the needs of an experiment, a straightforward method consists of performing a benchmark test with a reference sample. However, the obtained data involves all beamline elements including the beam optics and the sample, and therefore it may not be interpreted directly in terms of detector performance only. Furthermore, it may be difficult or impossible to transpose the results to other applications.

2. Detector characterization

Hence the need for a common basis for the description of an area detector in order to give detector users of different horizons a consistent understanding of the performances of a detector. Such a description should be application-independent as well as technology-independent in order to be applicable to any experiment and to any detector type. Finally this leads to considering a detector on the basis of its pure imaging characteristics only, these being defined as quantities derivable from image data only given a known input stimulus and applicable to any detector. From the point of view of a synchrotron beamline user, an X-ray area detector is generally a device that detects an X-ray photon beam of given energy with a certain efficiency, and that measures its intensity as a function of position in a two-dimensional space and as a function of time with a certain accuracy. An area detector may

therefore be fully characterized by its efficiency and by its measuring range and accuracy for each of the intensity, position and time variables. These elements are generally quantified by the following parameters, which will be defined in more detail in the following sections:

(i) Detection efficiency: readout noise, detective quantum efficiency (DQE).

(ii) Intensity resolution: gain, non-linearity, digital encoding range, dynamic range, dark signal, image blemishes.

(iii) Position (or spatial) resolution: field geometry, spatial sampling pitch, line-spread function (LSF), contrast or modulation transfer function (CTF or MTF), spatial distortions.

(iv) Time resolution: as regards area detectors for synchrotron experiments, time resolution generally refers to the achievable repetition rate when acquiring a sequence of frames. It is therefore most often described by the detector frame rate at minimum exposure time, dead-time for readout, and exposure time range.

Being established from the most general definition of an area detector, this set of parameters completely describes, and is applicable to, almost any area detector, except perhaps for very specific implementations which are out of the scope of this paper. For this reason, many area detector characterization reports in the literature deal with this same parameter list. As stated above, a benchmark test with a reference sample cannot substitute for the imaging characterization but can usefully complete it in order to confirm the detector performance in the targeted application. Detector characterization data are exploited for instance in the following situations:

(i) Selection of a detector for a given experiment.

(ii) Acceptance testing for a newly purchased detector.

(iii) Quantitative comparison between different detector systems.

(iv) Check for detector performance drift in time.

(v) Investigate possible detector fault in case of poor data quality.

3. Measurement methods

Owing to the large variability of detector systems and of experimental conditions at synchrotron facilities, the establishment of measurement standards such as those used in medical imaging, for instance the IEC-62220-1 for DQE measurements, is practically impossible. Procedures described in this section are practical examples to be adapted depending on particular situations, and do not exclude alternative methods. Whatever the method, it should comply with the following guidelines in order to be applicable to any detector type and to virtually any on-site configuration:

(i) The only required data are the detector input stimulus and the corresponding output image.

(ii) Only basic image processing is necessary.

(iii) Only simple tools and standard X-ray instrumentation are needed.

The measurements assume a monochromatic incoming radiation, so the incoming X-ray photon flux is a relevant input signal unit for energy-integrating as well as for photon-counting detectors. Measurements should be made on the image format that the users will use in practice, *i.e.* on corrected images if the system provides online flat-field and distortion corrections as this is the case for instance on large-area CCD detectors for macromolecular crystallography, or on raw images otherwise. On systems with online data corrections, raw images can nevertheless provide useful additional system information but they are not available in all cases.

3.1. Gain

The gain G of an area detector can be defined as the ratio of the integrated image signal to the corresponding integrated signal at the detector input. The image signal is expressed in analog-to-digital units (ADU). For monochromatic beams the input signal is best described by the amount of X-ray quanta at the detector input. The gain serves for image data rescaling into units of incident X-ray flux and is an indicator of the system sensitivity, so it is sometimes also called the conversion ratio or sensitivity. Commercial sheets generally either do not specify it or give an estimate derived from system components characteristics, thus it is never known precisely so it is essential to calibrate it. The gain is sometimes defined as the image signal per absorbed (instead of incident) photon. However, the signal per absorbed photon is not measurable in the general case, except for photon-counting systems and for highly sensitive integrating detectors with single photon detection capability. Therefore this gain definition is of restricted scope and is not considered here.

The usual measurement set-up at ESRF is shown in Fig. 1. A fluorescing scatterer placed on the sample stage is used as a secondary source creating a large cone beam (Moy *et al.*, 1996). For macromolecular crystallography detectors for instance, the used scatterer is a lithium glass with Ge-doping generating a relatively homogeneous scattered beam at 9.8 keV main energy (Ge fluorescence). The beam is collimated with a pinhole and the X-ray flux through the pinhole is first calibrated with a scintillation counter. The pinhole must be made of a totally absorbing material, for instance 0.5 to 1 mm Pb for energies up to 40 keV. The X-ray flux is adjusted within the counter linear operating range, typically 50000 counts s^{-1} or below, by using pinholes of different diameters, and by adjusting the pinhole-to-scatterer distance. For an insertion device source and uniform filling mode the pinhole diameter and its distance to the scatterer are typically

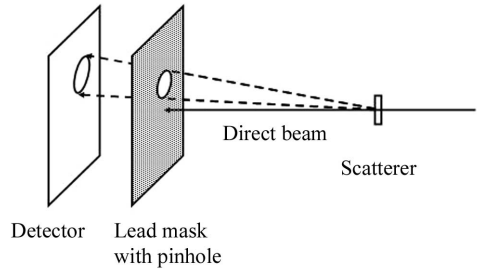

Figure 1
Gain measurement layout.

a few tenths of a mm and a few tens of cm, respectively. Then the counter is replaced by the detector which is placed at about the same distance from the pinhole as was the counter, and an image of the pinhole is taken. A dark image is taken at the same exposure time and subtracted from the image in order to eliminate the dark offset. Then the gain G in ADU/incident photons is given as

$$G = \left[\sum_{\mathrm{ROI}} I(i,j) \right] \Big/ NT, \qquad (1)$$

where ROI is an image region of interest containing the entire pinhole spot image, $I(i, j)$ is the value of pixel (i, j) in the dark-subtracted image, N is the count rate through the pinhole measured with the scintillating counter, and T is the exposure time of the pinhole image. This method ensures that both the calibrating counter and the detector under test receive exactly the same X-ray flux, thereby avoiding data renormalization inaccuracies. For a well defined beam energy the proportion of elastic scatter in the cone beam should be reduced to a minimum by tuning the beam energy above and as close as possible to the fluorescing element K-edge. With horizontally polarized beams, as is most often the case with synchrotron sources, the elastic scatter may even be virtually eliminated by placing the detector orthogonally to the direct beam axis. If, owing to on-site constraints, none of these methods are applicable, care should be taken to at least place the pinhole solid angle out of the main elastic scattering rings of the fluorescing sample. On a bending-magnet source with low ring currents the intensity of the so-produced cone beam may be too low, leading to exaggerated exposure times. In that case one may try to use the direct beam with sufficient collimation and attenuation. With undulator or wiggler sources, gain calibration with the direct beam is delicate because strong attenuation is necessary. Beam attenuation with thick absorbers increases the relative intensity of higher-order harmonics so is not recommended. Beam attenuation by detuning the monochromator second crystal allows both the beam intensity and the proportion of harmonics to be reduced but may not provide sufficient attenuation in all cases.

The gain of a CCD-based crystallography detector is typically around 1 ADU/X-ray at 10 keV. The gain decreases above a certain energy owing to absorption loss in the phosphor screen.

3.2. Gain inhomogeneity

The local gain calibration described above may be completed by a map of gain variations across the detector surface. However, this requires either exposing the detection area to a perfectly homogeneous beam, which may be difficult for a large-area system, or performing a time-consuming detector surface scanning with a perfectly stable or precisely monitored beam. A large cone beam, even if not perfectly uniform over the whole detection area, nevertheless allows one to diagnose and to some extent quantify various gain homogeneity defects, for example an imperfect gain balance between quadrants of mosaic CCD systems (Fig. 2), or a phosphor screen edge delamination. For diffraction systems a

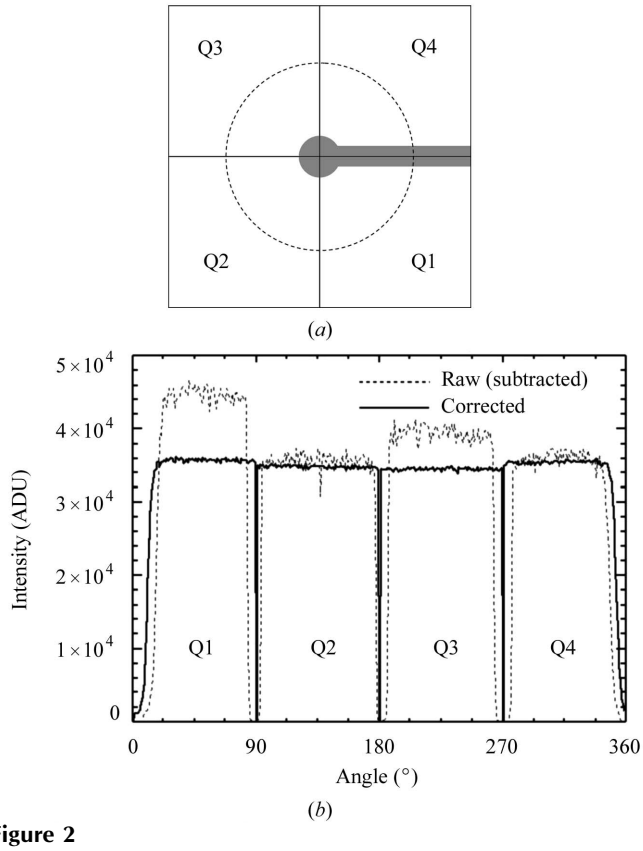

Figure 2
Gain inhomogeneity map (partial image) of a 2 × 2 mosaic fiber-optic taper input CCD detector. (*a*) Detector input layout. (*b*) Image levels along dotted circle in image (*a*) for raw and corrected images. The flood-field beam is not perfectly homogeneous radially but has central symmetry, allowing the difference in gain between each quadrant to be measured by taking the intensity profile along a circle. The residual non-homogeneity between each quadrant is measured to be 5%.

gain inhomogeneity of 2% (±1% with respect to the average value) or less in corrected images is deemed acceptable.

3.3. Integral non-linearity

The integral non-linearity is an important factor since most quantitative experiments require 1% or better precision in X-ray flux measurements. However, a linearity measurement over the whole detector range with better than 1% precision requires precise instrumentation and is time-consuming. In case a full linearity characterization cannot be performed it is suitable to at least check the linearity at high input levels in order to detect possible saturation effects. For detector field widths of a few cm or more and for energies up to a few tens of keV, this can be done by taking the image of an aluminium step-wedge with 10–20 steps typically 50 µm thick placed on the detector input window and using a homogeneous beam as for the gain measurement. The detector field around the step-wedge must be completely shielded with lead foils. The exposure time and beam intensity are set so as to reach the maximum image level in the thinnest part of the step-wedge. A dark image of the same exposure time is subtracted from the step-wedge image. The incoming beam and the detector

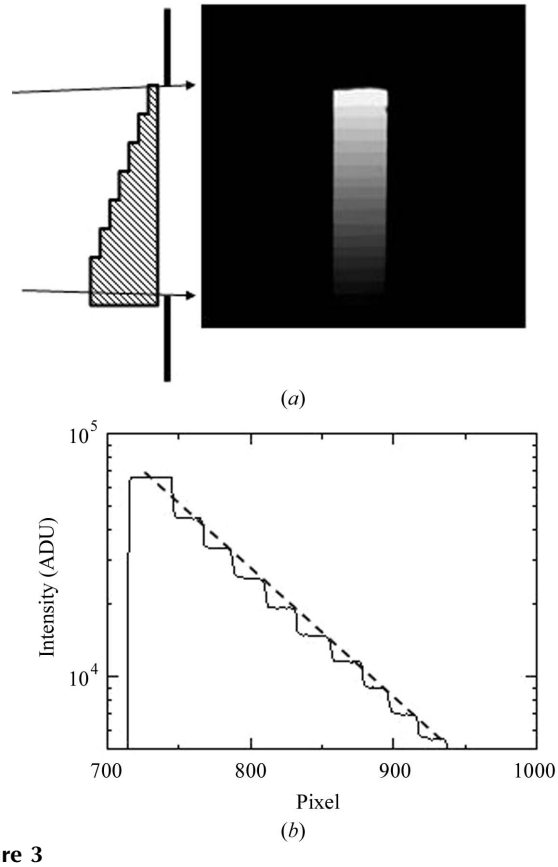

Figure 3
Linearity of a CCD detector with fiber-optic taper input. (*a*) Image of an aluminium step-wedge with 50 µm-thick steps. (*b*) Step-wedge cross section after dark subtraction, in logarithmic scale. The upper step is slightly higher showing a non-linear response at high level. It was checked that this effect does not appear in the raw image, confirming that the problem originates from image correction.

response must be homogeneous over the exposed area. Plotting the cross section of the step-wedge transmission image in logarithmic scale allows non-linear effects to be detected (Fig. 3), since for monochromatic radiation such a profile should show equally spaced steps owing to Beer's law. For CCD systems the test allows a quick diagnosis of for instance flat-field rescaling errors at high level (as is the case in Fig. 3) or CCD full-well saturation. For counting systems it could be used to estimate the equivalent dead-time. For small-field (a few mm wide) high-resolution detectors the above method may be difficult to implement; in this case the linearity may be measured by exposing the detector to the direct beam and varying the beam intensity at constant exposure time with sufficient precision, taking precautions as explained in §3.1.

3.4. Encoding range

This parameter is generally specified as analog-to-digital converter (ADC) bits for signal integrating detectors or as counter depth in bits for event detectors, so no measurement is necessary. It should not be confused with the dynamic range, which represents the portion of actually usable encoding range as will be detailed in §3.7. Most CCD systems used on beamlines have encoding ranges between 12 bits and 16 bits. Large encoding ranges, being obtained at the expense of readout speed, are generally incompatible with high frame rates.

3.5. Dark-image noise, readout noise

Dark-image noise is commonly defined as the standard deviation of pixel values in a small (typically 100×100 pixels) region of interest (ROI) of a dark image. Dark-image noise σ_d is a combination of random readout noise σ_r and of non-random dark signal non-uniformity (DSNU) σ_{DSNU}, combining quadratically: $\sigma_d^2 = \sigma_r^2 + \sigma_{DSNU}^2$. Most area detectors provide online dark-field subtraction, thereby cancelling the DSNU so only the readout noise σ_r remains in the corrected image. If only raw images are available, one must eliminate the DSNU as well for consistency by subtracting two dark images of the same integration time. The noise in the subtracted image, σ_{sub}, is such that $\sigma_{sub}^2 = 2\sigma_r^2$ so the readout noise is obtained as $\sigma_r = \sigma_{sub}/(2^{1/2})$. The readout noise should be measured for exposure times representative of the system used, that is for instance about 1 s for slow-scan CCD cameras or 0.1 s for fast frame-rate cameras and so forth. Readout noises obtained from corrected and from raw images can be different owing to possible image-level rescaling by flat-field correction, so the type of image used must be mentioned. For a CCD system, a dark noise of around 1.5–2 ADU/pixel r.m.s is a typical good value. A noise higher than 4 ADU/pixel r.m.s. may result from internal gain oversetting which is detrimental to dynamic range, or from a larger than necessary ADC encoding range which is detrimental to readout speed.

Given a known gain G the readout noise σ_r can be converted into a noise-equivalent input flux, $\sigma_{eqX} = \sigma_r/G$, allowing direct comparison of the noise of different detectors. The readout noise in equivalent input photons also provides an order of magnitude of the lowest detectable input signal; however, there is no unique relationship between both, in this matter each application uses its own criteria. The typical noise equivalent for a CCD detector with large-area fiber-optic input is 1–3 X-rays/pixel r.m.s. at 10 keV. Intensified CCDs and direct-detection CCDs have input noises well below 1 X-ray/pixel r.m.s., thereby allowing for single X-ray detection.

3.6. Dark signal

It is difficult to define a standard dark signal measurement because dark signal structure is system-dependent. Usually a dark image consists of some bright pixels randomly scattered on a more or less uniform background. The dark background level usually increases with integration time. Hence the dark signal can generally be quantified by the average background increase rate in ADU s^{-1} and by the number of so-called hot pixels, *i.e.* those pixels with anomalous dark signal. Various criteria can define a hot pixel: for instance, dark signal higher than ten times the average background increase rate, or dark signal higher than 0.1% of the maximum encoding range at the nominal exposure time, or any other equivalent definition.

Should there be any drift in time of the dark background average level at constant exposure time, it must be quantified because this will affect the detector accuracy for low incident X-ray flux.

3.7. Dynamic range

The dynamic range is defined as the ratio of maximum signal within the linear range to the minimum detectable signal, the latter being defined for instance as the r.m.s. readout noise in signal integrating systems and as one count in photon-counting systems. It is generally expressed in bits (logarithm base 2). As outlined before, the dynamic range must not be confused with the ADC encoding range. Some, but not all, detector commercial sheets now indicate both quantities in order to avoid misleading interpretations. CCD systems for macromolecular diffraction generally have a dynamic range between 13.5 and 15.5 bits for an ADC range of 16 bits.

3.8. Spatial resolution

The spatial resolution of an area detector can be described either by the line spread function (LSF) or point spread function (PSF) or in the Fourier domain by the modulation transfer function (MTF) or contrast transfer function (CTF). Since the spatial resolutions of synchrotron area detectors range from submicrometer to a few hundreds of micrometers there is no unique spatial resolution measurement method. For spatial resolutions of a few tens of µm or larger, a LSF profile may be directly obtained as the cross section of the image of a thin beam collimated with sharp slits. The slits should be placed as close as possible to the detector input. Generally the orthogonal slit cross section does not contain enough pixels for an accurate LSF FWHM measurement, but this can be overcome using the tilted slit method (Fujita *et al.*, 1992): a tilt angle θ of the slit with respect to the pixel matrix is equivalent to oversampling the LSF profile by a factor $1/\sin(\theta)$. The obtained profile (Fig. 4*a*) represents the system LSF before sampling by the pixel matrix. For a relevant measurement using this method, the slit length should be at least several tens of pixels. If this cannot be achieved with the direct beam, one can use a secondary source as for the gain measurement and place a slit on the detector entrance window, but this can lead to long exposure times. For micrometric or submicrometric resolutions this method is hardly applicable, at least with standard slits. In this case, special tools and methods must be used (Koch *et al.*, 1999): special slits, derivative of the cross section of a sharp edge transmission image (also applicable to large-field systems), deconvolution of an interference pattern image acquired in coherent mode. One may also suggest the deconvolution of the cross section of the transmission image of a thin tungsten wire of known diameter.

In addition to the LSF FWHM it is useful to know the LSF width at 10% and 1% of maximum, particularly for diffraction or for small-angle scattering. For this purpose several orthogonal cross sections of the slit image are summed to improve the signal-to-noise ratio at low level (Fig. 4*c*). The obtained profile shows the LSF tails extension as well as the practical dynamic range, and therefore contains a lot of information on the system; should there be only one plot in the tests results, it should probably be this one. Long LSF tails are characteristic

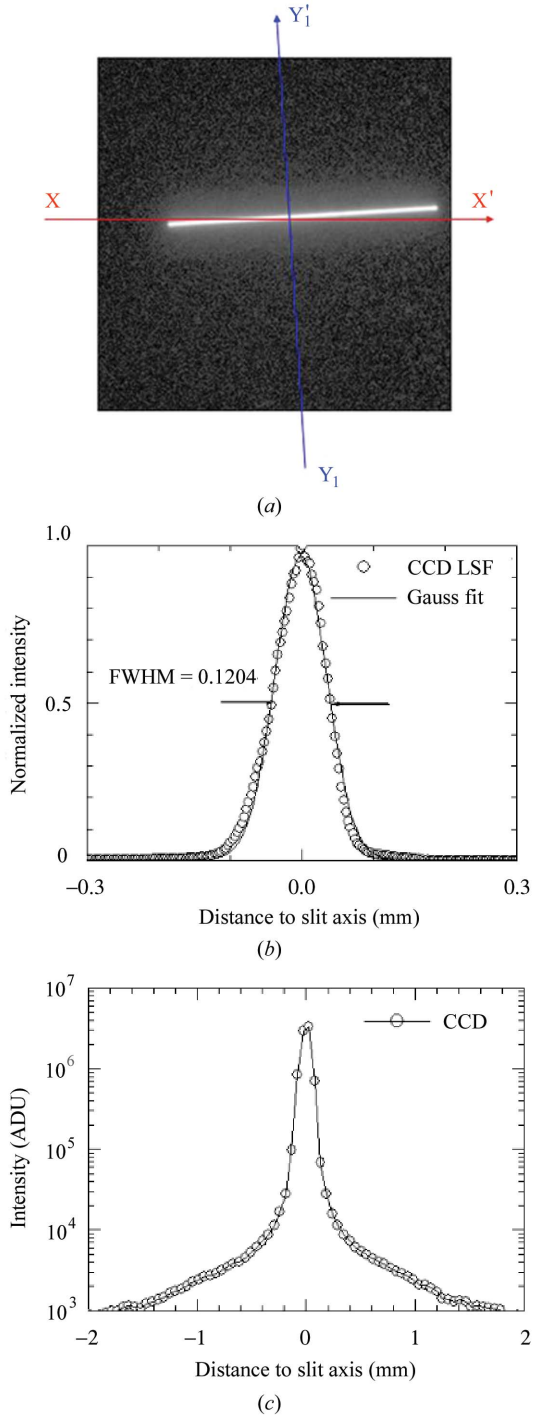

Figure 4
LSF measurement on a lens-coupled CCD detector. (*a*) Dark-subtracted image of a thin slit, tilt angle 3.4° with respect to pixel direction XX′, image levels on logarithmic scale. (*b*) Single cross section along XX′ providing the pre-sampling LSF FWHM. (*c*) Summed cross sections along YY′ (orthogonal to the slit) showing the LSF tails down to less than 10^{-3} relative intensity levels.

of optically coupled CCD detectors and in that case are due to light scatter in the optical elements and in the phosphor screen. Semiconductor detectors with direct X-ray to electric signal conversion are not prone to this problem and have sharper LSFs; in these cases the observed LSF tails may reflect the X-ray beam collimation imperfections rather than the detector spatial response. This leads to the general remark whereby the beam quality can become a critical issue when characterizing high-performance detectors. Generally the detector spatial resolution can be considered isotropic so a LSF measurement in arbitrary orientation is sufficient. Otherwise the LSF should be measured in different orientations. Rather than measuring the LSF, it is possible to measure the PSF by taking a cross section in the image of a pinhole. It should be noted that LSF and PSF profiles are not equivalent so it is important to be precise about which one is measured. In the practical point of view the LSF method is preferable to the PSF method because a small PSF spot is more difficult to distinguish from hot pixels or various image blemishes than a LSF image, especially on large-area systems.

The CTF is obtained as the orthogonal cross section in the image of a lead bar pattern (*e.g.* Huttner) with different bar spacings (Fig. 5). As for the LSF measurement there is an advantage in slightly tilting the bar pattern with respect to the pixels alignment in order to oversample the contrast modulation profile, especially for detectors with a sharp spatial response. Some commercial detector sheets indicate MTF or CTF values in line-pairs per mm, referring to the 'limiting resolution' or the 'maximum resolution'. However, these quantities are essentially subjective and their definition varies depending on the detector supplier; therefore they are not valid for quantitative detector comparisons. For consistency with the LSF FWHM it is rather suggested to record as a CTF (or MTF) figure the spatial frequency in line-pairs per mm closest to the 50% CTF (or MTF) cut-off. Unlike the CTF, the MTF cannot be measured directly because it would require absorption patterns with sinusoidal transmission profiles which are difficult to make for X-rays. The MTF can be obtained by discrete Fourier transform of the pre-sampling LSF. The MTF may also be derived from discrete CTF values (Holst, 1998), but this is less straightforward.

For synchrotron detectors the LSF width is more often used than the MTF or the CTF for spatial resolution characterization because it directly provides a length scale of the detectable details. However, imaging scientists in the medical field are more acquainted with the MTF (Bravin *et al.*, 2004). Hence it is useful to provide both LSF and CTF (or MTF) data, at least the LSF FWHM and the spatial resolution at 50% CTF (or MTF) cut-off.

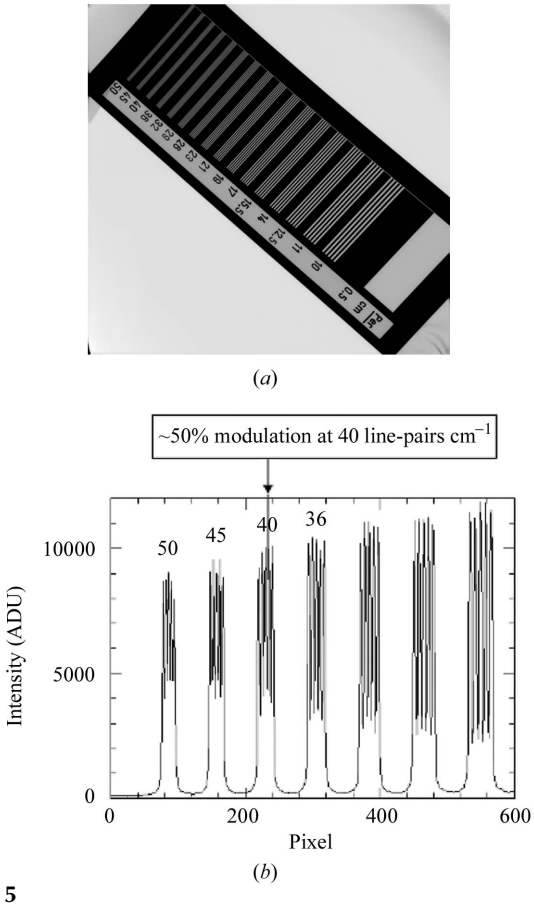

Figure 5
CTF of a fiber-optic taper CCD detector with 100 mm × 100 mm input field. (*a*) Image of the resolution bar pattern after flat-field correction. (*b*) Cross section. The line frequency closest to 50% modulation is easily identified.

3.9. Detective quantum efficiency

The detective quantum efficiency, earlier introduced by Gruner *et al.* (1978) for X-ray area detectors, is formally defined as

$$\mathrm{DQE} = \left(S_{\mathrm{out}}^2/\sigma_{\mathrm{out}}^2\right)/\left(S_{\mathrm{in}}^2/\sigma_{\mathrm{in}}^2\right). \qquad (2)$$

where S_{out} and σ_{out} are the average signal and the noise at the system output (*i.e.* in the image), and S_{in} and σ_{in} are the average signal and the noise at the system input (*i.e.* in the incident beam). The DQE is nowadays agreed as a reference figure of merit for an X-ray area detector, in both medical and scientific fields. For a perfect noiseless detector the DQE is equal to its mean absorption quantum efficiency QE. For a real system the DQE is equivalent to the QE of a perfect detector which would give the same image statistics for the same input flux. Unlike the QE, which is a characteristic of the X-ray conversion medium and is generally not accessible to measurement, the DQE is a system parameter that can be in principle measured on any detector. In (2), $\sigma_{\mathrm{in}}\sigma_{\mathrm{out}}$ may be thought of as either a spatial or a time fluctuation, leading to different measurement methods. In any case, for a relevant DQE derivation the output fluctuations have to be calculated on a set of non-correlated data acquired under the same conditions. In the space domain for instance, considering that $S_{\mathrm{out}}/S_{\mathrm{in}} = G$ by definition of gain G and that $\sigma_{\mathrm{in}} = S_{\mathrm{in}}^{1/2}$ owing to Poisson statistics, expression (2) can be rewritten as

$$\mathrm{DQE} = GS_{\mathrm{out}}/\sigma_{\mathrm{out}}^2, \qquad (3)$$

thereby expressing the DQE as a function of measurable quantities: image level S_{out}, image noise σ_{out} and gain G. The

general DQE measurement procedure (Tate *et al.*, 1995) based on this expression is implemented as follows:

(i) Acquire two large field images at an exposure level significantly (typically 100 to 1000 times) higher than the r.m.s. readout noise and at the same energy as for the gain measurement.

(ii) Subtract the large field images to suppress any non-random trend correctable by flat-field correction and divide the result by $2^{1/2}$ for noise normalization to a single image.

(iii) Rebin the subtracted image with sufficiently large pixels, typically 16×16 or more, so that the influence of the MTF on signal variance can be neglected, calculate image noise $\sigma_{\rm out}$ in a homogeneous image region of typically 10×10 rebinned pixels or more.

(iv) Take as $S_{\rm out}$ the average image signal for rebinned pixels in the same image region as for $\sigma_{\rm out}$.

This procedure, applicable to virtually any detector, provides a first-order estimate of the DQE at zero spatial frequency with minimum computing and instrumentation. Considering that the precision on gain G is about $\pm 10\%$, one can assume the uncertainty on the DQE measurement to be about $\pm 15\%$ at best.

The variance $\sigma^2_{\rm out}$ may also be calculated in the time domain from successive exposures of a spot of constant intensity (Tate *et al.*, 1995; Stanton *et al.*, 1992), but this requires perfectly stable beam intensity, position and exposure, and requires many images to be processed.

Expressing (3) in the Fourier domain (Granfors *et al.*, 2001) leads for instance to the following expression,

$$\mathrm{DQE}(\nu) = \frac{G S_0\, \mathrm{MTF}(\nu)^2}{N\, \mathrm{NPS}_0(\nu)}, \qquad (4)$$

where G is the gain, S_0 is the average image signal per pixel, MTF is the pre-sampling modulation transfer function, NPS_0 is the azimuthal integration of the two-dimensional image noise power spectrum (assumed isotropic), N is the number of points in $\mathrm{NPS}_0(\nu)$ and in $\mathrm{MTF}(\nu)$ discrete spectra, and ν is the discrete spatial frequency. Other expressions derived from the measured CTF are also proposed (Stierstorfer & Spahn, 1999), avoiding the MTF calculation. But in any case this requires the calculation of the image NPS (Aufrichtig *et al.*, 2001) and hence time and computing power. Therefore the measurement of the spatial-frequency-dependent DQE is rather reserved for detailed detector studies (Ponchut *et al.*, 2005; Koch, Macherel *et al.*, 2001) whereas the zero frequency DQE determination from equation (3) is appropriate for routine detector characterization. Both methods were applied to characterize the DQE of a photon-counting pixel array detector (Fig. 6) for comparison with other detector systems. It can be verified that both methods give consistent results at zero spatial frequency. The detector DQE at zero frequency was found to be close to its theoretical quantum absorption efficiency, QE = 0.35, at the same energy.

Experience shows that the DQE measurement is sometimes delicate: the result is sensitive to X-ray exposure as well as to detector response inhomogeneities. For too inhomogeneous images the DQE estimate at zero spatial frequency does not converge for increasing pixel rebinning size so is not reliable. Hence a careful measurement set-up is necessary, and it is useful to double-check the result by performing several independent measurements.

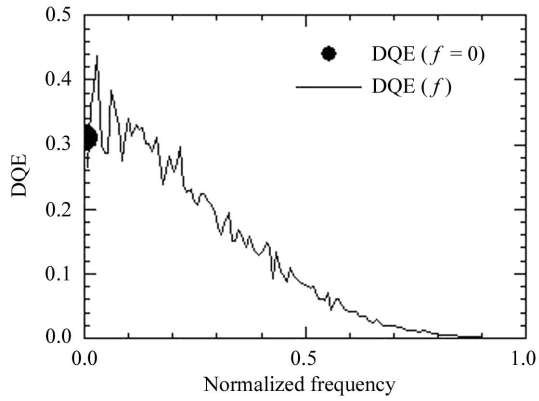

Figure 6
DQE of a photon-counting pixel array (Medipix2) at 17.4 keV. Plot: DQE as a function of spatial frequency calculated using expression (4). Black dot: direct DQE estimation from rebinned images calculated with expression (3). Both methods give consistent results at zero spatial frequency.

3.10. Geometrical distortions

Optical coupling and in particular fiber-optic tapers introduce geometrical image distortions of various aspects: continuous field distortions like barrel, pin-cushion, trapezoid, as well as field discontinuities like shear distortion (Fig. 7). The former is factory calibrated using a grid mask and corrected online by applying the inverse distortion field to the raw images. The latter is due to imperfect fiber-optic structure or correction algorithm. In routine evaluation the continuous field distortion, or gross distortion $D_{\rm gross}$, is calculated as the maximum variation in demagnification ratio g across the input field: $D_{\rm gross} = (g_{\rm max} - g_{\rm min})/(g_{\rm mean})$. This is measured in different ways depending on the distortion field. Typical

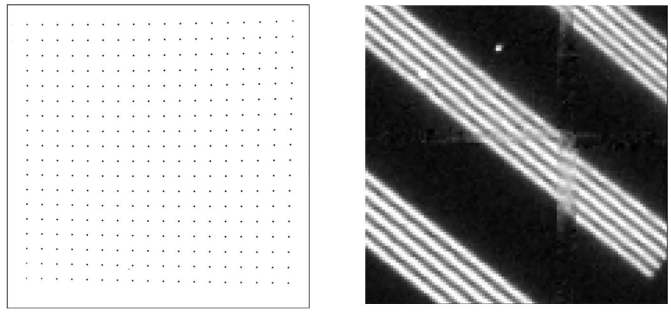

Figure 7
Geometrical distortions typical of CCD detectors with demagnifying fiber-optic input. (*a*) Image of a gridhole mask showing gross distortion with trapezoid shape. (*b*) Corrected image of a multi-taper CCD system, showing shear distortion at the taper's edge (detail view). The shear was due to the distortion correction and could be further suppressed by using a grid with finer pitch for distortions calibration.

distortions are 3–4% for fiber-optic tapers and less than 1% for high-quality tandem lens couplers. Shear distortion is quantified as the amount and length of shears. Shears can appear within the taper surface or at the edge of two tapers and can be made visible with a line-patterned absorbing object (Fig. 7*b*). Since it is practically impossible to probe the entire detector surface for shears in a routine test, shear distortion can be specified as the maximum shear length observed and possibly the shear density over a small area.

3.11. Image blemishes

In the most general sense an image blemish is an image area with abnormal pixel values. Hence a blemish specification aims at defining what is an abnormal pixel value and at enumerating the occurrences of various morphological arrangements of such pixels in an image. The definition of image blemishes below is based on specifications for CCD detectors with fiber-optic inputs, but is applicable to virtually any area detector:

(i) Pixel defect: a pixel with normal dark signal (*i.e.* excluding hot pixels) but with less than 50% or more than 150% response compared with the average image level in a uniformly illuminated image.

(ii) Cluster defect: a group of contiguous pixel defects.

(iii) Column defect: a group of contiguous pixel defects aligned within one single column.

The upper and lower image level thresholds for a pixel defect represent the limits for efficient flat-field correction, hence they are somewhat arbitrary and may be set differently. This general definition may be completed by more specific image blemish descriptions if appropriate. As an example, a typical blemish specification for a 1k × 1k X-ray CCD detector is given in Table 1, and may be easily adapted to different image sizes. Specification of an image blemish grade is a delicate balance between system cost, industrial state-of-the-art and actual experimental needs.

Table 1
Example of image blemishes specification.

Cluster > 50 pixels	None
Cluster 10–49 pixels	0 in zone 1, 1 in zone 2, 4 in zone 3 (Fig. 8)
Columns defects	≤ 1 in zone 1, ≤ 2 elsewhere
Hot pixels density	$\leq 10^{-3}$

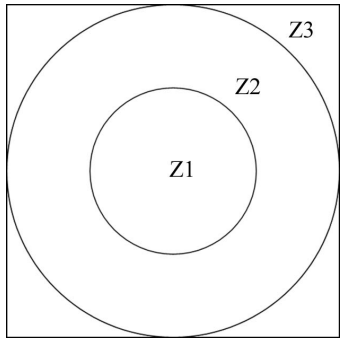

Figure 8
Image areas for blemish specification. Z1: centered circle, diameter = field side/2; Z2: centered ring, (field size/2) < diameter < field size; Z3: area outside Z2.

3.12. Frame rate

The detector frame rate can be simply calculated from the duration of an acquisition sequence of several images at zero or minimum exposure time. The frame rate after detector integration to the beamline may differ from the specifications due to possible delays introduced by network connections or by external triggering. Frame rate also depends on whether the acquisition sequence includes online data correction and hard-disk data storage. In case the detector is affected by signal persistence effects, as is the case for amorphous silicon flat panels for instance, the amount of signal lag at maximum frame rate should be measured, as well as the frame rate for which the signal lag between two successive images is lower than a certain threshold (*e.g.* lower than 10^{-3} relative level).

3.13. Dead-time for readout

Dead-time for readout is obtained as the difference between acquisition cycle time and integration time. As for the frame rate, the data-collection conditions have to be mentioned. Readout dead-time may depend on exposure time, for instance for systems with double-buffered data output (readout while integrating).

3.14. Image-processing tools

The above detector characterization methods can be carried out using image-processing software providing the following features: (i) image subtraction, addition; (ii) image rebinning; (iii) image rotation; (iv) image ROI; (v) image thresholding; (vi) image display linear and logarithmic; (vii) cross-sections graphs on linear and on logarithmic scale; (viii) statistical tools: ROI average, standard deviation, histogram.

The detector acquisition and display software generally provide most of these features. If not, the software should allow the image data to be exported to a raw binary format or to a commonly used image format like TIFF (tagged image file format) for further processing with an imaging software like, for instance, *Fit2D* (Hammersley, 1993).

4. Detector characterization examples

To illustrate the above description, Table 2 and Fig. 9 give as an example the characteristics measured on the FReLoN CCD camera with fiber-optic taper input developed at the ESRF (Labiche, 2004). A number of X-ray area detector characterization reports can be found in the literature. Here are only a few examples: fiber-optic tapered CCD (Naday *et al.*, 1994; Phillips *et al.*, 2002), lens-coupled CCD (Koch, 1994; Moy, 1994), integrating pixel arrays (Glasser *et al.*, 1996; Rossi *et al.*, 1999), photon-counting pixel arrays (Ponchut *et al.*, 2005), amorphous silicon flat panel (Granfors *et al.*, 2001).

Table 2
Measured characteristics of the FreLoN 2k16 CCD detector with fiber-optic input. The input screen is a 39 μm-thick P43 powder blend. The X-ray source is a molybdenum anode X-ray tube with 25 kVp high voltage and 100 μm Zr filtration, providing a quasi-monochromatic X-ray beam with 174 keV energy.

Test conditions	
X-ray source	Mo X-ray tube, 25 kVp voltage, 100 μm Zr filtration
X-ray energy	17.4 keV
Detector	CCD cooling 253 K
Tests data	
Detection field	94 mm × 94 mm, 46 μm pixels
Gain	1.3 ADU/X-ray
Gain inhomogeneity	1.4% p–p gain variation between the four quadrants
Readout noise	4.2 ADU r.m.s. at 5 s exposure
Saturation level	∼65400 ADU
Encoding range	16-bit ADC
Dark signal	$\sim 1.2 \times 10^4$ hot pixels (>1 ADU pixel^{-1} s^{-1}); dark pedestal (image offset) = 1000 ADU
Dynamic range	(65400–1000)/4.2 ≃ 14-bit
Non-linearity	Linear response up to the ADC saturation level
Spatial resolution	CTF 50% = 4 line-pair mm^{-1}; LSF FWHM = 124 μm; LSF FW10%M = 258 μm
Image distortion	∼4% peak-to-peak variation of demagnification ratio
Image blemishes	One taper blemish, 0.7 mm × 0.35 mm
Frame rate (theoretical)	4 frames s^{-1} maximum in full resolution; 8 frames s^{-1} in 2 × 2 binning

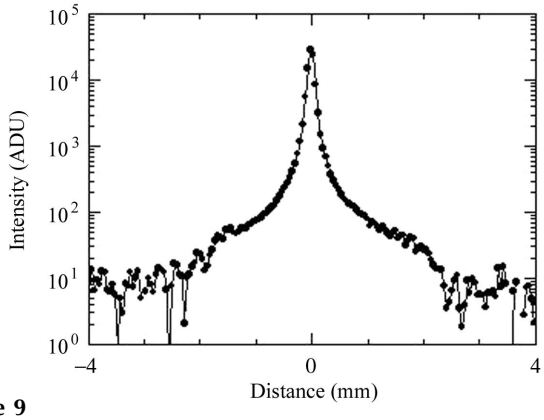

Figure 9
LSF of FreLoN system. The slit width is 20 μm, the X-ray beam energy is 17.4 keV (Zr-filtered Mo X-ray tube).

5. Conclusion

The general methodology for characterization of X-ray area synchrotron detectors has been reviewed. It is based on a common set of imaging parameters that can be measured on practically any detector. Measurement methods attached to each parameter cannot be standardized due to the wide variety of synchrotron detectors, but guidelines for consistent and relevant measurement procedures can be drawn. This parametric description of a detector provides quantitative data to help choose the relevant detector equipment for any application. Furthermore, it can be used as a tool to facilitate information exchange among the detector users and the detector developers in the synchrotron community. It is hoped that this review can contribute to continuously improve the performance of X-ray detector equipment at synchrotron beamlines. Another aim is to incite further activity regarding efficient X-ray area detector evaluation, *e.g.* in the development of dedicated software tools for image data analysis.

References

Aufrichtig, R., Su, Y., Cheng, Y. & Granfors, P. R. (2001). *Proc. SPIE*, **4320**, 362–372.

Bérar, J. F., Blanquart, L., Boudet, N., Breugnon, P., Caillot, B., Clemens, J. C., Delpierre, P., Koudobine, I., Mouget, C., Potheau, P. & Valin, I. (2002). *J. Appl. Cryst.* **35**, 471–476.

Bravin, A., Fiedler, S., Coan, P., Nemoz, C., Fernandez, M., Adam, J. F., Ponchut, C. & Labiche, J. C. (2004). *IEEE Nuclear Science Symposium, Satellite Workshop on Synchrotron Radiation Detectors*, 22 October 2004, Rome, Italy.

Broennimann, C., Eikenberry, E. F., Horisberger, R., Huelsen, G., Schmitt, B., Schulze-Briese, C. & Tomizaki, T. (2003). *Nucl. Instrum. Methods*, A**510**, 24–28.

Fujita, H., Tsai, D.-Y., Itoh, T., Doi, K., Morishita, J., Ueda, K. & Ohtsuka, A. (1992). *IEEE Trans. Med. Imag.* **11**, 34–39.

Glasser, F., Campagnolo, R., Mathy, F., Louis, N. & Mermet, L. (1996). *Nucl. Instrum. Methods*, A**380**, 252–255.

Granfors, P. R., Aufrichtig, R., Possin, G. E., Gianbattista, B. W., Huang, Z. S., Liu, J. & Ma, B. (2001). *Med. Phys.* **27**, 1324–1331.

Gruner, S. M., Milch, J. R. & Reynolds, G. T. (1978). *IEEE Trans. Nucl. Sci.* **25**, 562–565.

Hammersley, A. (1993). *Fit2D Reference Manual.* ESRF, Grenoble, France.

Holst, G. C. (1998). *CCD Arrays, Cameras and Displays*, 2nd ed. Winter Park, FL: JCD Publishing.

Koch, A. (1994). *Nucl. Instrum. Methods*, A**348**, 654–658.

Koch, A., Cloetens, P., Ludwig, W., Labiche, J. C. & Ferrand, B. (1999). *Proceedings of the 5th Conference on Inorganic Scintillators and their Applications (SCINT99)*, 16–20 August 1999, Moscow, Russia.

Koch, A., Macherel, J. M., Wirth, T., Groot, P. d., Ducourant, T., Couder, D., Moy, J. P. & Calais, E. (2001). *Proc. SPIE*, **4320**, 115–120.

Koch, M. H. J., Boulin, C., Briquet-Laugier, F., Epstein, A., Sheldon, S., Beloeuvre, E., Gabriel, A., Hervé, C., Kocsis, M., Koschuch, A., Laggner, P., Leingartner, W., Iseli, C. d. R., Reimann, T., Golding, F. & Torki, K. (2001). *Nucl. Instrum. Methods*, A**467–468**, 1156–1159.

Labiche, J. C. (2004). *IEEE Nuclear Science Symposium, Satellite Workshop on Synchrotron Radiation Detectors*, 22 October 2004, Rome, Italy.

Lewis, R. A., Helsby, W. I., Jones, A. O., Hall, C. J., Parker, B., Sheldon, J., Clifford, P., Hillen, H., Sumner, I., Fore, N. S., Jones, R. W. M. & Roberts, K. M. (1997). *Nucl. Instrum. Methods*, A**392**, 32–41.

Moy, J. P. (1994). *Nucl. Instrum. Methods*, A**348**, 641–644.

Moy, J. P., Hammersley, A., Svensson, S. O., Thompson, A., Brown, K., Claustre, L., Gonzales, A. & McSweeney, S. (1996). *J. Synchrotron Rad.* **3**, 1–5.

Naday, I., Westbrook, E. M., Westbrook, M. L., Travis, D. J., Stanton, M., Phillips, W. C., O'Mara, D. & Xie, J. (1994). *Nucl. Instrum. Methods*, A**348**, 635–640.

Phillips, W. C., Stewart, A., Stanton, M., Naday, I. & Ingersoll, C. (2002). *J. Synchrotron Rad.* **9**, 36–43.

Ponchut, C. & Zontone, F. (2003). *Nucl. Instrum. Methods*, A**510**, 29–34.

Ponchut, C., Zontone, F. & Graafsma, H. (2005). *IEEE Trans. Nucl. Sci.* **52**, 1760–1765.

Rossi, G., Renzi, M., Eikenberry, E. F., Tate, M. W., Bilderback, D., Fontes, E., Wixted, R., Barna, S. & Gruner, S. M. (1999). *J. Synchrotron Rad.* **6**, 1096–1105.

Stanton, M., Philips, W. C., Li, Y. & Kalata, K. (1992). *J. Appl. Cryst.* **25**, 638–645.

Stierstorfer, K. & Spahn, M. (1999). *Med. Phys.* **26**, 1312–1319.

Tate, M. W., Eikenberry, E. F., Barna, S. L., Wall, M. E., Lowrance, J. L. & Gruner, S. M. (1995). *J. App. Cryst.* **28**, 196–205.